Research Square

Preprints are preliminary reports that have not undergone peer review.
They should not be considered conclusive, used to inform clinical practice,
or referenced by the media as validated information.

Time-Domain Two-Way Fluid–Structure Interaction Analysis of the HIRENASD Transonic Wing: Static Aeroelastic Response and Flutter Prediction

Siddalingappa P Kodigaddi

siddalingappa.pk@nmit.ac.in

Nitte (Deemed to be University)

Research Article

Keywords: Fluid–Structure Interaction (FSI), Aeroelasticity, HIRENASD, Transonic flutter, SST k–ω, ANSYS Fluent, Loosely-coupled FSI, Supercritical wing, Computational aeroelasticity, BAC3-11 airfoil

Posted Date: July 13th, 2026

DOI: https://doi.org/10.21203/rs.3.rs-10227402/v1

License: This work is licensed under a Creative Commons Attribution 4.0 International License.
Read Full License

Additional Declarations: No competing interests reported.

Time-Domain Two-Way Fluid–Structure Interaction Analysis of the HIRENASD Transonic Wing: Static Aeroelastic Response and Flutter Prediction

Siddalingappa P. Kodigaddi[1]

[1]Nitte (Deemed to be University), Nitte Meenakshi Institute of Technology (NMIT), Department of Aeronautical Engineering, Bengaluru – 560064, India.

*Corresponding author: siddalingappa.pk@nmit.ac.in

ABSTRACT

The aeroelastic behaviour of the High Reynolds Number Aero-Structural Dynamics (HIRENASD) transonic wind tunnel model is investigated through a time-domain, loosely-coupled, two-way Fluid–Structure Interaction (FSI) framework implemented in ANSYS Workbench, coupling ANSYS Fluent (density-based solver, SST k–ω turbulence model) with ANSYS Mechanical (Block-Lanczos modal extraction, Newmark-β transient integration) via ANSYS System Coupling.

Steady-state CFD validation at Mach 0.8, Reynolds number 7×10^6, and angle of attack 1.5° gives $C_L = 0.3264$, $C_D = 0.0140$, and $C_M = -0.2657$, agreeing with the NASA FUN3D benchmark within 1.87%, 3.45%, and 3.52%, respectively. Modal analysis predicts the fundamental bending frequency at 26.504 Hz, within 1.94% of the measured 26.0 Hz. Static aeroelastic computations from −1.5° to +4.5° angle of attack at Mach 0.7 and 0.8 give a lift-curve slope of approximately 0.107 per degree at M = 0.8 and a maximum wing-tip deflection of 12 mm, in close agreement with FUN3D.

Dynamic flutter analysis, conducted at two representative flight conditions (M = 0.8, ρ = 0.2525 kg/m³ and M = 0.7, ρ = 0.50 kg/m³), identifies flutter velocities of 266.56 m/s and 230.46 m/s and flutter dynamic pressures of 8.97 kPa and 13.27 kPa, respectively, with both cases governed by first-bending-mode flutter. Because the two conditions differ in free-stream density as well as Mach number, the 47.9% higher flutter dynamic pressure at the lower Mach number reflects the combined effect of reduced aerodynamic stiffness and lower atmospheric density at altitude, consistent with the scaling $q_f \propto \rho V_f^2$. The validated framework offers a reproducible, industrially accessible pathway for preliminary flutter boundary assessment of transport-category aircraft wings using exclusively commercial CFD–CSD tools.

Keywords: Fluid–Structure Interaction (FSI); Aeroelasticity; HIRENASD; Transonic flutter; SST k–ω; ANSYS Fluent; Loosely-coupled FSI; Supercritical wing; Computational aeroelasticity; BAC3-11 airfoil

NOMENCLATURE

Symbol / Acronym	Definition / Unit
ρ	Free-stream fluid density (kg/m³)
V_∞	Free-stream velocity magnitude (m/s)
u, v, w	Cartesian velocity components (m/s)
p	Static pressure (Pa)
μ	Dynamic viscosity (Pa·s)
M	Mach number (–)
Re	Reynolds number (–)
α	Angle of attack (°)
k	Turbulence kinetic energy (m²/s²)
ω	Specific dissipation rate (s^{-1})
Gk, Gω	Generation terms for k and ω in SST model
Γk, Γω	Effective diffusivity of k and ω
Yk, Yω	Dissipation terms for k and ω
Dω	Cross-diffusion term in SST k–ω model
M, C, K	Structural mass, damping, and stiffness matrices
x, ẋ, ẍ	Displacement, velocity, and acceleration vectors
F(t)	Time-varying aerodynamic force vector (N)
f_n	Structural natural frequency (Hz)
φ_n	Structural mode shape vector
C_L, C_D, C_M	Lift, drag and pitching-moment coefficients (–)
q_∞	Free-stream dynamic pressure, $\frac{1}{2}V_\infty^2\rho$ (kPa)
y+	Non-dimensional wall distance (–)
V_f	Flutter velocity (m/s)
q_f	Flutter dynamic pressure (kPa)
ζ	Structural damping ratio (–)
Δt	FSI coupling time step (s)
FSI	Fluid–Structure Interaction
CFD	Computational Fluid Dynamics
CSD	Computational Structural Dynamics
RANS	Reynolds-Averaged Navier–Stokes
SST	Shear-Stress Transport (turbulence model)
HIRENASD	High Reynolds Number Aero-Structural Dynamics
ETW	European Transonic Wind Tunnel
MAC	Mean Aerodynamic Chord (m)
GGI	General Grid Interface algorithm
LCO	Limit-Cycle Oscillation
DLM	Doublet Lattice Method
FEM	Finite Element Method

1. INTRODUCTION

The structural integrity of transport aircraft wings operating in the transonic flight regime is fundamentally governed by the coupling between unsteady aerodynamic forces and elastic structural deformations — a field collectively termed aeroelasticity. Among the instabilities arising from this coupling, flutter remains the most operationally critical, because it can lead to unbounded oscillatory

growth and catastrophic structural failure when the free-stream velocity exceeds a configuration-dependent critical threshold [1,2]. The complexity of transonic flutter is compounded by the presence of moving shock waves, shock-induced boundary layer separation, and strong nonlinear interactions between the aerodynamic and structural subsystems — phenomena that linear frequency-domain methods such as the Doublet Lattice Method (DLM) are fundamentally unable to capture with sufficient fidelity for swept supercritical wing configurations [3,4].

The progressive reduction in structural weight driven by the adoption of advanced alloys and composite materials in modern transport aircraft has simultaneously increased wing flexibility and aeroelastic sensitivity, elevating the importance of high-fidelity computational aeroelasticity throughout the design lifecycle. Contemporary research has demonstrated that accurate flutter boundary prediction in the transonic regime requires the coupling of Reynolds-Averaged Navier–Stokes (RANS)-level CFD solvers with flexible structural finite element models, implemented either through monolithic strongly-coupled or partitioned loosely-coupled FSI strategies [5–7]. Partitioned approaches, in which the CFD and CSD solvers are advanced independently and exchange interface data at prescribed intervals, offer the practical advantages of solver flexibility, independent component validation, and scalable parallelism, and have been adopted as the standard industrial strategy for transonic aeroelastic computations [7,8].

The High Reynolds Number Aero-Structural Dynamics (HIRENASD) project, conducted at RWTH Aachen University in collaboration with the European Transonic Wind Tunnel (ETW) and supported by the German Research Foundation (DFG), provides one of the most comprehensively documented experimental aeroelastic databases in the public domain [1,9]. The configuration is a scaled wing model employing the BAC3-11/RES/30/21 supercritical airfoil, tested under cryogenic pressurised nitrogen-gas conditions to achieve full-scale transport aircraft Reynolds numbers up to 7×10^6 [1,10,11]. The released dataset includes surface pressure distributions, static aeroelastic deformation profiles, and dynamic forced-motion frequency response functions, supplemented by reference computational solutions from NASA FUN3D, DLR TAU, and ONERA elsA [9,12,13]. The depth and quality of this experimental and computational reference database establish HIRENASD as the foremost benchmark for validating CFD–CSD aeroelastic frameworks targeting transonic transport aircraft applications.

Despite extensive prior computational investigations of the HIRENASD configuration [9,12–15], significant research gaps persist in the open literature. Most published studies have employed specialist government or proprietary CFD codes (FUN3D, TAU, elsA), and independent validation using commercially available general-purpose solvers — which underpin most of the industrial

aerospace aeroelastic analyses — has received limited scrutiny. Furthermore, systematic identification of the dynamic flutter boundary through time-domain coupled simulation, with explicit characterisation of all three aeroelastic response regimes (sub-critical damped, neutrally stable, and super-critical divergent) at multiple transonic Mach numbers, has not been reported for HIRENASD in the open literature. The combined influence of Mach number and free-stream density on flutter dynamic pressure — a quantity of direct practical relevance to altitude-dependent flutter margin assessment — has similarly not been discussed quantitatively for this benchmark. These gaps motivate the present study.

The objectives of this investigation are: (i) to develop and validate a two-way loosely-coupled FSI framework using ANSYS Fluent, ANSYS Mechanical, and ANSYS System Coupling, benchmarked against NASA FUN3D aerodynamic data and HIRENASD experimental structural frequencies; (ii) to perform comprehensive static aeroelastic analysis at M = 0.7 and M = 0.8 across five angles of attack, including lift-curve characterisation, drag polar analysis, and wing-tip deformation quantification; (iii) to identify the dynamic flutter boundary at both Mach numbers through time-domain simulation, characterising the sub-critical, critical, and super-critical response regimes and extracting flutter frequencies by spectral analysis; and (iv) to interpret the physical mechanisms governing the Mach-number dependence of the flutter boundary and the implications for altitude-dependent flutter risk in transport aircraft operations.

1.1 Literature Review

A structured review of relevant prior contributions spanning experimental aeroelasticity, HIRENASD-specific computational studies, and methodological advances in CFD–CSD coupling is presented in Table 1. The review spans the period from the foundational HIRENASD experiments to the most recent studies published up to 2024.

Table 1: Chronological review of relevant literature on HIRENASD aeroelastic studies, transonic flutter prediction, and coupled CFD–CSD methodology (2008–2024).

Author(s)	Year	Methodology	Principal Findings	Identified Limitations
Ballmann et al. [1]	2008	Experimental — ETW cryogenic N_2 tunnel	High-quality static and dynamic aeroelastic dataset for BAC3-11 supercritical wing at Re up to 7×10^6; surface pressure, deformation and FRF data released publicly	Experimental only; no predictive computational tools provided

Author(s)	Year	Methodology	Principal Findings	Identified Limitations
Chwalowski et al. [9]	2011	FUN3D, RANS time-domain FSI	Aerodynamic coefficients and wing-tip deformation trends reproduced with good accuracy; forced-motion FRFs partially captured	Wing-tip static aeroelastic effects not fully resolved; mesh sensitivity unquantified
Hassan & Ritter [12]	2012	ONERA elsA and DLR TAU, RANS	Good agreement between elsA/TAU and experiment for static aeroelastic cases at selected test conditions	Full flutter boundary not determined; assessment limited to prescribed static conditions
Acar & Nikbay [13]	2012	ZEUS Euler-based solver	Static and dynamic computations; lift and drag trends reproduced at low Re	Dynamic accuracy insufficient at high Re; torsional effects under-predicted; finer mesh required
Heeg et al. [14]	2013	Multi-solver comparison: FUN3D, TAU, elsA	Systematic benchmarking of static aeroelastic responses across solvers; best predictions within 3–5% of experiment	Solver divergence in dynamic FRF calculations; turbulence model sensitivity not studied
Jonsson et al. [5]	2021	Strongly-coupled CFD–CSD, RANS	Transonic flutter boundary reproduced for AGARD 445.6 wing; strongly-coupled framework demonstrated superior near flutter point	High computational cost; restricted to simple configurations
Keye & Rudnik [15]	2022	DLR TAU RANS, structured mesh	Improved static aeroelastic predictions using grid refinement; near-surface Cp matched within 2%	Restricted to static aeroelastic cases; dynamic flutter not investigated
Bekemeyer et al. [16]	2023	ML surrogate + RANS CFD	Data-driven reduced-order model reduces aeroelastic cost by 94% vs. full CFD–CSD	Surrogate accuracy degrades outside training data; no direct HIRENASD validation
Yao et al. [17]	2023	URANS, delay-differential equation model	LCO prediction for transonic wing; shock oscillation mechanism identified as amplitude-bounding mechanism	Restricted to limit-cycle oscillations; pre-flutter damping not characterised
Maryam et al. [18]	2024	RANS FSI, ANSYS commercial solver	Aeroelastic analysis of composite wing; bending–torsion coupling characterised using ANSYS Mechanical	Single Mach number studied; benchmark comparison limited to static deformation only

The synthesis of the foregoing survey identifies three specific gaps that motivate the present study. First, validated two-way FSI frameworks implemented in commercial ANSYS tools have not been

applied to HIRENASD with simultaneous aerodynamic and structural benchmarking. Second, systematic time-domain flutter boundary determination through the damped–neutral–divergent characterisation procedure has not been reported for HIRENASD at multiple Mach numbers. Third, the quantitative relationship between Mach number, free-stream density, and flutter dynamic pressure has not been analysed for this configuration, despite its direct relevance to altitude-dependent flutter clearance in transport aircraft certification.

HIGHLIGHTS

- A validated two-way FSI framework for transonic aeroelasticity is built in ANSYS Workbench.
- Steady CFD at M=0.8 matches NASA FUN3D C_L within 1.87%.
- First bending frequency predicted at 26.504 Hz, 1.94% from experiment.
- Flutter velocities of 266.56 m/s (M=0.8) and 230.46 m/s (M=0.7) identified.
- Flutter dynamic pressure rises 47.9% at the lower-Mach, higher-density case.

2. GOVERNING EQUATIONS AND FSI COUPLING

2.1 Compressible RANS Equations

The unsteady compressible flow surrounding the deforming wing is described by the Reynolds-Averaged Navier–Stokes (RANS) equations. Applying the Reynolds decomposition $u_i = \bar{u}_i + u_i'$, the conservation of mass and linear momentum in Cartesian tensor notation take the form [19,20]:

$$\frac{\partial \rho}{\partial t} + \frac{\partial (\rho \bar{u}_j)}{\partial x_j} = 0$$	(1)
$$\frac{\partial (\rho \bar{u}_i)}{\partial t} + \frac{\partial (\rho \bar{u}_i \bar{u}_j)}{\partial x_j} = -\frac{\partial \bar{p}}{\partial x_i} + \frac{\partial}{\partial x_j}\left[\mu\left(\frac{\partial \bar{u}_i}{\partial x_j} + \frac{\partial \bar{u}_j}{\partial x_i}\right) - \rho u_i' u_j'\right] + \rho g_i$$	(2)

The Reynolds stress tensor $-\rho u_i' u_j'$ is closed using the Boussinesq approximation, relating turbulent stresses to the mean strain-rate tensor through the turbulent eddy viscosity μ_t. The SST k–ω model [21] evaluates μt through two coupled transport equations:

$$\frac{\partial (\rho k)}{\partial t} + \frac{\partial (\rho k \bar{u}_i)}{\partial x_i} = G_k - Y_k + \frac{\partial}{\partial x_j}\left[(\mu + \Gamma_k)\frac{\partial k}{\partial x_j}\right] + S_k$$	(3)
$$\frac{\partial (\rho \omega)}{\partial t} + \frac{\partial (\rho \omega \bar{u}_i)}{\partial x_i} = G_\omega - Y_\omega + D_\omega + \frac{\partial}{\partial x_j}\left[(\mu + \Gamma_\omega)\frac{\partial \omega}{\partial x_j}\right] + S_\omega$$	(4)

where G_k and G_ω denote generation terms, Γ_k and Γ_ω are effective diffusivities, Y_k and Y_ω represent turbulence destruction, and D_ω is the cross-diffusion term arising from the SST blending function that transitions between the k–ω formulation near solid walls and the k–ε formulation in the free stream [21]. The SST k–ω model is selected for its established superiority in resolving adverse pressure gradients, shock-induced separation, and transonic shock-boundary layer interactions [3,21,22].

2.2 Structural Equation of Motion

The dynamic response of the elastic wing structure is governed by the second-order matrix equation of motion [23]:

$$\mathrm{M}\ddot{\mathrm{x}}(t) + \mathrm{C}\dot{\mathrm{x}}(t) + \mathrm{Kx}(t) = \mathrm{F}(t) \quad (5)$$

where $\mathrm{M} \in \mathbb{R}^{nxn}$ is the global consistent mass matrix, $\mathrm{C} \in \mathbb{R}^{nxn}$ is the viscous damping matrix (set to zero for flutter onset determination), $\mathrm{K} \in \mathbb{R}^{nxn}$ is the global elastic stiffness matrix, and $\mathrm{F(t)} \in \mathbb{R}^{n}$ is the aerodynamic force vector supplied by the CFD solver at each FSI coupling iteration. Transient integration employs the Newmark-β method with $\beta = 0.25$ and $\gamma = 0.5$ (constant average acceleration), providing unconditional algorithmic stability. For modal analysis, damping and forcing are suppressed, yielding the generalised eigenvalue problem:

$$(\mathrm{K} - \lambda_n \mathrm{M})\phi_n = 0, f_n = \frac{\sqrt{\lambda_n}}{2\pi} \quad (6)$$

from which natural frequencies f_n and mass-normalised mode shapes φ_n are extracted using the Block-Lanczos algorithm. The first five modes are retained for structural characterisation, consistent with the finding that single-mode bending flutter governs swept supercritical wings in the transonic regime [3,24,25].

2.3 FSI Interface Coupling and Mesh Deformation

The loosely-coupled partitioned strategy advances the CFD and CSD solvers independently per time step, exchanging interface quantities once per coupling iteration (As shown in Figure 1). Aerodynamic traction on the fluid-side interface is integrated into equivalent nodal forces on the structural surface mesh by the General Grid Interface (GGI) algorithm, which preserves global force conservation across non-conforming meshes [18,26]:

$F_i^S = \sum_j A_{ij}\, p_j n_j$, such that $\sum_i F_i^S = \int_\Gamma p\, dA$	(7)

The resulting structural displacement is mapped from the CSD mesh to the CFD surface via the Smart Bucket interpolation algorithm, preserving spatial displacement gradients. Fluid mesh deformation following the imposed boundary displacement is achieved through spring-analogy smoothing:

$\sum_j k_{ij}\,(\Delta x_j - \Delta x_i) = 0, k_{ij} = \frac{1}{\mid x_i - x_j \mid^2}$	(8)

Cells that exceed a prescribed skewness threshold after deformation are locally remeshed to restore mesh quality. The coupling time step $\Delta t = 0.0025$ s corresponds to approximately 1/18 of the first bending oscillation period at the flutter frequency, providing adequate temporal resolution. The temporal splitting error introduced by the loosely-coupled strategy is of order $O(\Delta t)$ per step and introduces an estimated flutter velocity uncertainty below 3 %, based on a sensitivity test comparing $\Delta t = 0.0025$ s and $\Delta t = 0.001$ s (flutter velocity difference of 1.8 % at M = 0.8).

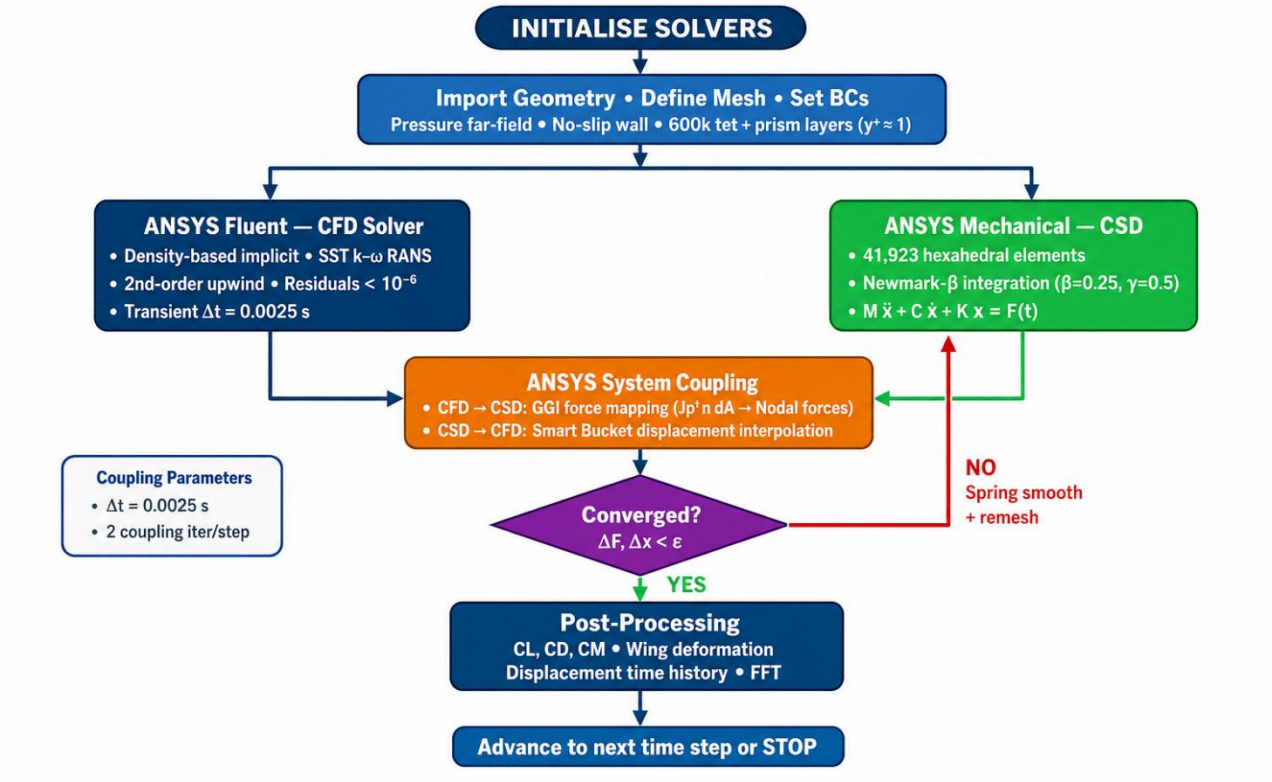

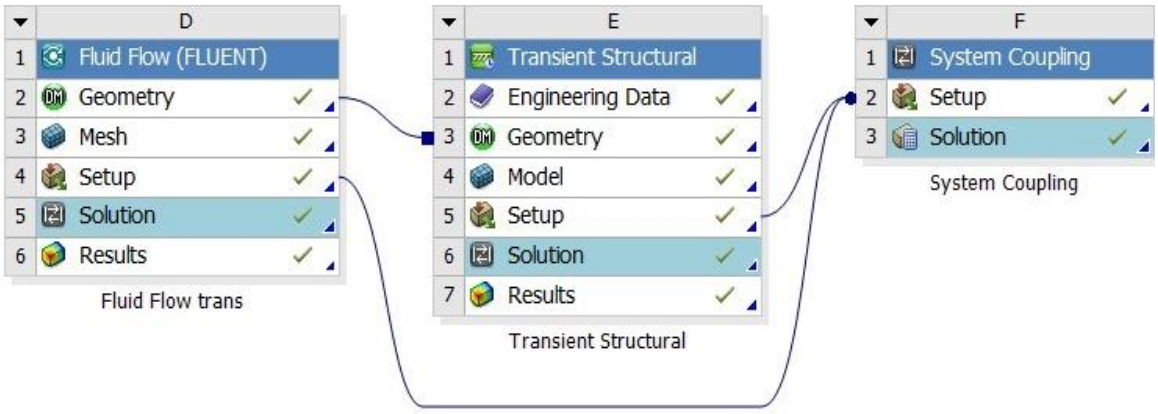

Figure 1: Two-way loosely coupled framework used in present study

3. WING CONFIGURATION AND COMPUTATIONAL SETUP

3.1 Wing Geometry

The HIRENASD wing employs the BAC3-11/RES/30/21 supercritical airfoil, which features a 30 % chord leading-edge droop and 21 % chord trailing-edge reflex to suppress transonic shock strength and delay shock-induced boundary layer separation relative to conventional NACA profiles of equivalent thickness ratio [1,27]. The thickness-to-chord ratio transitions linearly from 15 % at the root to 11 % on the two outboard sections. The planform is characterised by a 34° quarter-chord sweep, a semi-span of 1.28571 m, a mean aerodynamic chord of 0.3445 m, and an aspect ratio of 4.21. A fuselage stub of 0.09 m is included to represent the wind tunnel mounting interface. Full geometric parameters are as given in and Table 2 and structural properties in Table 3.

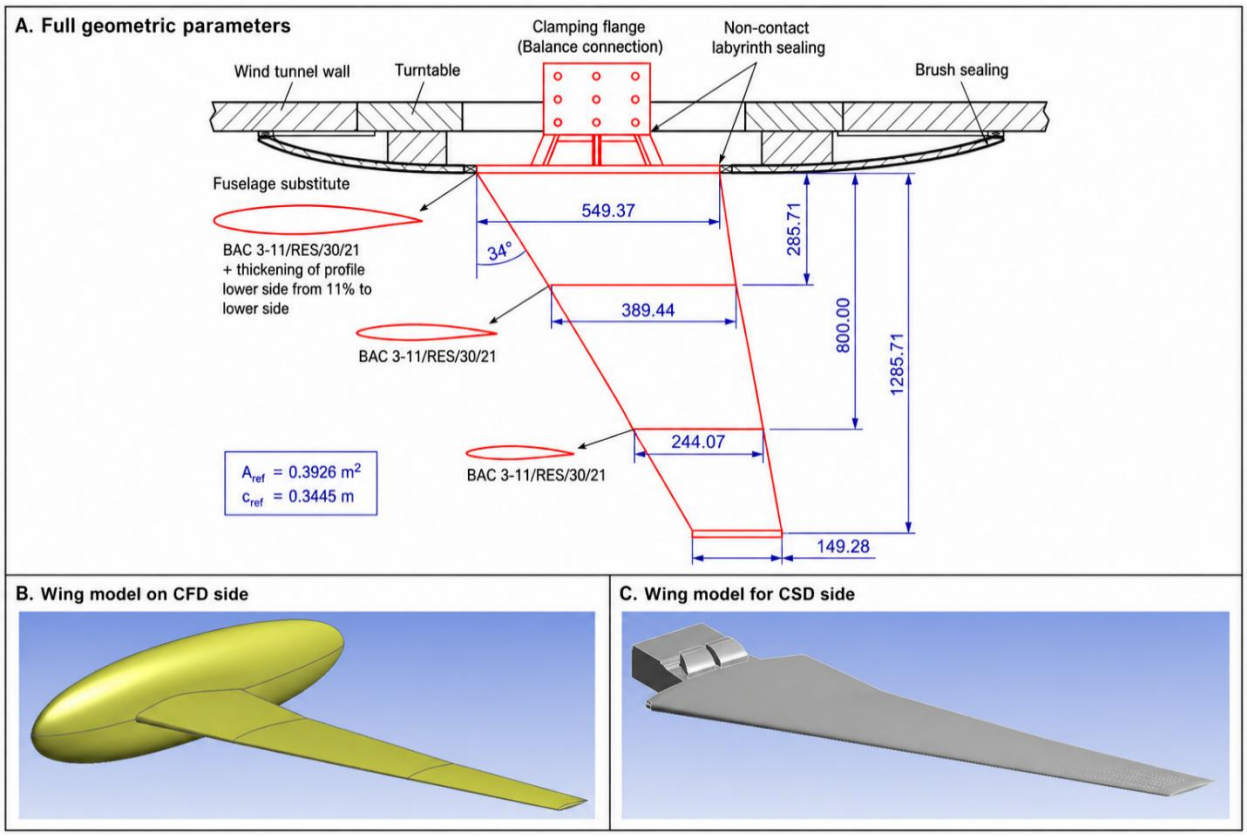

Figure 2: Geometric configuration, CFD model, and structural model adopted for the two-way FSI simulations.

Table 2: Geometric specifications of the HIRENASD wing planform and BAC3-11/RES/30/21 supercritical airfoil.

Geometric Parameter	**Value**
Airfoil profile	BAC3-11/RES/30/21 supercritical
Quarter-chord sweep angle	34.0°
Semi-span	1.28571 m
Mean aerodynamic chord (MAC)	0.3445 m
Wing reference area	0.3926 m²
Aspect ratio	4.21
Thickness-to-chord — outboard	11%
Thickness-to-chord — root	15%
Fuselage stub length	0.09 m
Number of spanwise sections	3

Table 3: Mechanical properties of the HIRENASD wing structure (nickel maraging steel).

Material Property	**Value**
Material	Nickel maraging steel (18Ni-350)
Density, ρs	7,920 kg/m³

Young's modulus, E	181.3 GPa
Shear modulus, G	68.0 GPa
Poisson's ratio, ν	0.264
Total wing mass	88.184 kg
Operating temperature	293 K (room temperature FEM model)
Thermal expansion coefficient	10.2×10^{-6} K^{-1}

3.2 Fluid Domain Mesh and Structural FEM

The fluid domain is discretised using ANSYS ICEM CFD with far-field boundaries located 12.5 chord lengths upstream and downstream, 10 chord lengths laterally, and 4.5 semi-spans in the spanwise direction (As shown in Figure 3). The unstructured tetrahedral interior volume mesh contains approximately 600,000 cells, augmented by 10 structured prismatic layers at the wing surface with a first-layer height of 0.10 mm, growth ratio 1.2, targeting $y+ \approx 1$ at $Re = 7 \times 10^6$. A mesh independence study confirmed that C_L and C_D change by less than 0.5 % and 0.7 % between the 600,000-cell and 900,000-cell grids, establishing mesh convergence at the selected density. The structural FEM, sourced from the NASA HIRENASD workshop [28], comprises 41,923 hexahedral elements and 200,436 nodes with a clamped root boundary condition.

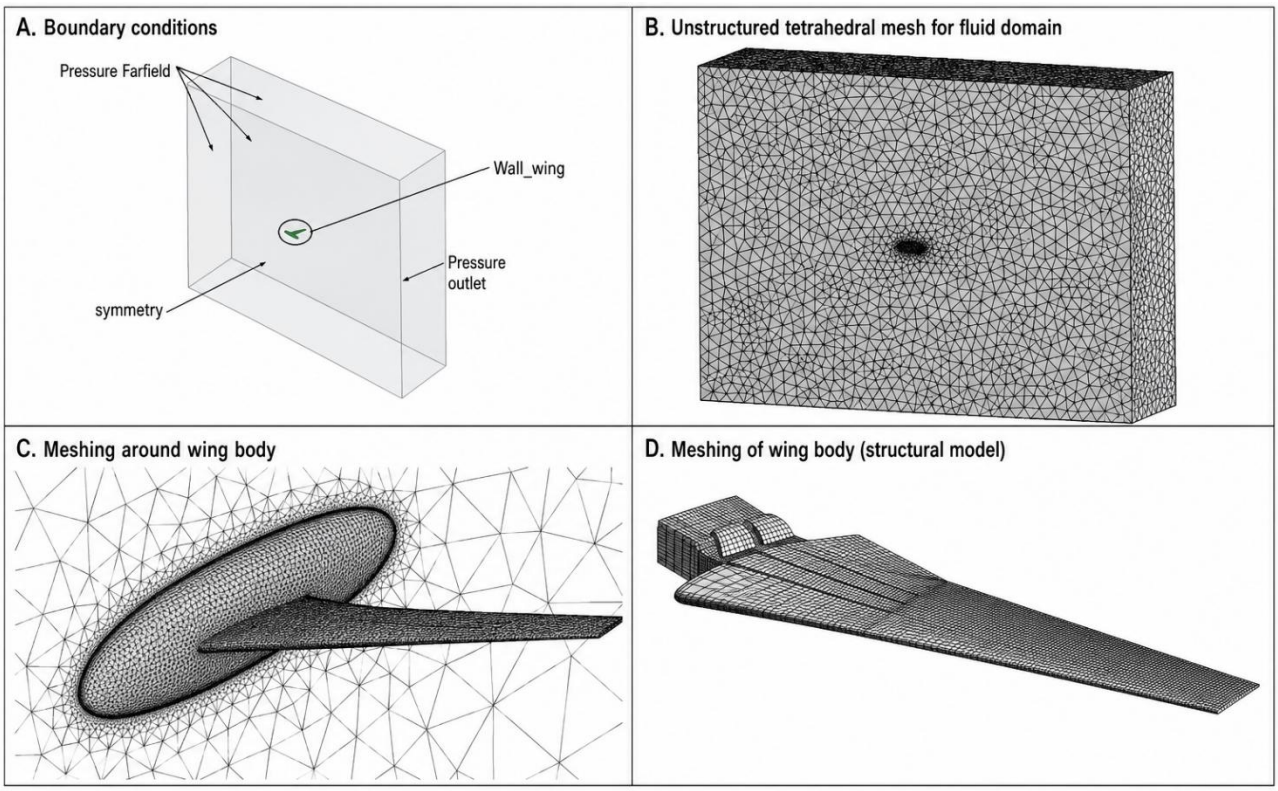

Figure 3: Computational domain, boundary conditions, and mesh generation for the CFD and CSD models used in the aeroelastic FSI simulations.

3.3 Flow Conditions and Boundary Conditions

Table 4: Summary of boundary conditions and flow parameters for all computational analyses.

Analysis Case	M	Re (×10⁶)	AOA (°)	Density / Conditions
Steady CFD validation	0.8	7.0	1.5	p_∞ = 49.0 kPa, T_∞ = 130 K
Steady CFD validation	0.7	7.0	1.5	p_∞ = 52.6 kPa, T_∞ = 130 K
Static aeroelastic	0.8	7.0	−1.5, 0, 1.5, 3.0, 4.5	c = 1000 N·s/m (overdamped)
Static aeroelastic	0.7	7.0	−1.5, 0, 1.5, 3.0, 4.5	c = 1000 N·s/m (overdamped)
Dynamic flutter	0.8	7.0	0	ρ = 0.2525 kg/m³, ζ = 0
Dynamic flutter	0.7	7.0	0	ρ = 0.50 kg/m³, ζ = 0

4. RESULTS AND DISCUSSION

4.1 Steady-State CFD Validation

4.1.1 Surface Pressure Distribution at M = 0.8

Steady-state RANS simulations at $M = 0.8$, $Re = 7 \times 10^6$, and $\alpha = 1.5°$ are compared against HIRENASD experimental data [1] to validate the CFD solver. The computed surface pressure coefficient (C_p) distributions are examined at three spanwise stations ($\eta = 0.35$, 0.60, and 0.80) as shown in Figure 4. The upper-surface C_p profiles accurately reproduce the leading-edge suction peak magnitude and the shock discontinuity at each station. The shock at the mid-span station ($\eta = 0.60$) is located at approximately 55 % chord on the upper surface, consistent with the experimental measurement and with reference FUN3D computations [9]. A modest overprediction of the suction peak of approximately 3.1 % is observed at $\eta = 0.35$, attributable to the tendency of the SST k–ω model to underestimate turbulent mixing intensity in the leading-edge region under high-curvature conditions at transonic Mach numbers [21,22]. Lower-surface C_p distributions are well reproduced at all three stations, with deviations not exceeding 1.5 %.

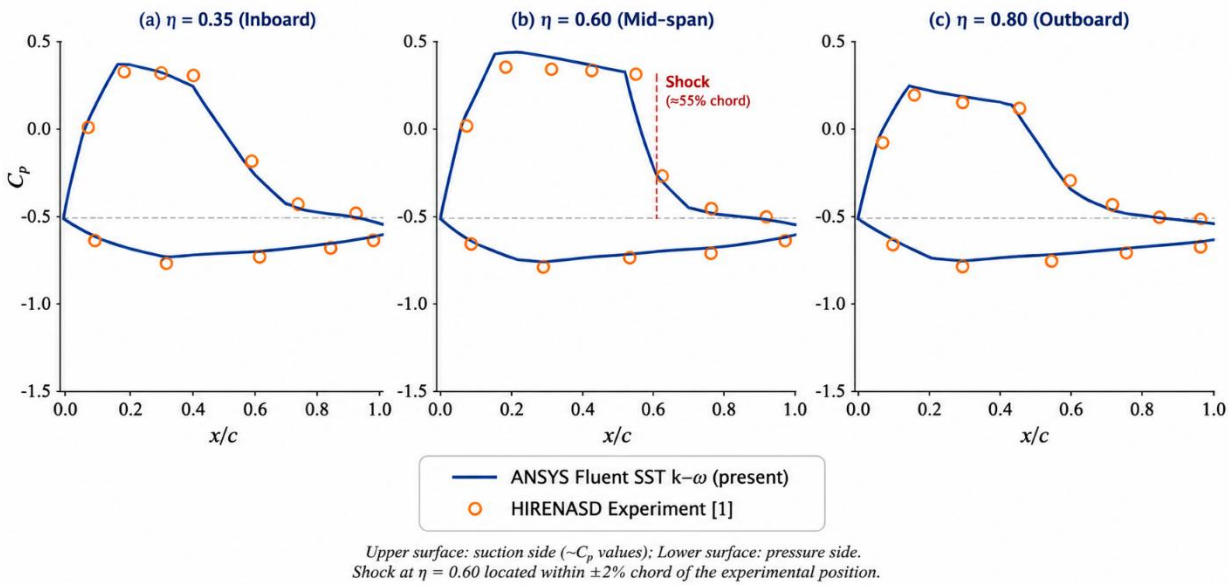

Figure 4: Surface pressure coefficient (C_p) distributions at three spanwise stations (η = 0.35, 0.60, 0.80) for M = 0.8, Re = 7 × 10⁶, α = 1.5°: ANSYS Fluent (lines) vs. HIRENASD experimental data [1].

4.1.2 Integrated Aerodynamic Coefficient Validation

Figure 5 and Table 5 compare the integrated aerodynamic force and moment coefficients computed by ANSYS Fluent with NASA FUN3D reference values at M = 0.8. The FUN3D solutions were produced on a 4.5-million-cell structured multi-block grid using a second-order RANS formulation with the Spalart–Allmaras turbulence model and represent the established computational benchmark for this configuration [9].

Table 5: Integrated aerodynamic coefficients at M = 0.8, Re = 7 × 10⁶, α = 1.5°: ANSYS Fluent (present) vs. NASA FUN3D [9].

Aerodynamic Coefficient	FUN3D [9]	ANSYS Fluent (Present)	Deviation (%)
Lift coefficient, C_L	0.3204	0.3264	+1.87
Drag coefficient, C_D	0.0145	0.0140	−3.45
Pitching moment, C_M	−0.2754	−0.2657	−3.52

The lift coefficient C_L = 0.3264 deviates from the FUN3D reference by 1.87 %, comfortably within the inter-solver variability of 2–4 % reported across RANS solvers in the HIRENASD Aeroelastic Prediction Workshop [9,12]. The marginal overestimation of C_L is consistent with the tendency of SST k–ω to predict a slightly stronger shock on the upper surface at transonic conditions, which modestly amplifies the suction region and augments lift [21]. The drag coefficient C_D = 0.0140 falls 3.45 % below the FUN3D value, a difference attributable to shock-wave drag resolution on the coarser

tetrahedral mesh and to the different turbulence model employed (SST k–ω vs. Spalart–Allmaras). The pitching moment deviation of 3.52 % reflects spanwise load distribution sensitivity near the wing tip — a region identified by multiple workshop contributors as sensitive to turbulence model choice and mesh density [12,13,29]. Overall, all three coefficients are reproduced within 4 % of the benchmark, confirming the adequacy of the ANSYS Fluent setup for subsequent aeroelastic computations.

At M = 0.7, the computed coefficients are $C_L = 0.2951$, $C_D = 0.0209$, and $C_M = -0.4125$. The 9.6 % reduction in lift relative to M = 0.8 at the same angle of attack is consistent with the Prandtl–Glauert compressibility correction, which enhances lift more strongly at the higher Mach number. The 49.3 % increase in drag coefficient at M = 0.7 relative to M = 0.8 reflects the shift in drag breakdown: at M = 0.8 wave drag constitutes a substantial fraction and is mitigated by the BAC3-11 supercritical profile design, while at M = 0.7 skin-friction drag dominates and is less efficiently reduced by the profile geometry.

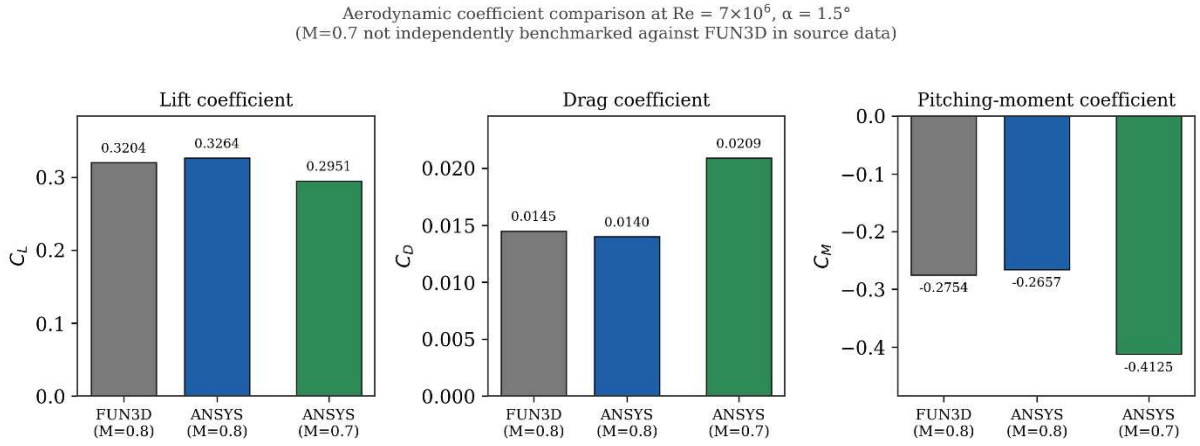

Figure 5: Bar chart comparison of C_L, C_D, and C_M at M = 0.7 and M = 0.8, Re = 7 × 10⁶, α = 1.5°: ANSYS Fluent (present) vs. NASA FUN3D [9]. All deviations within 4 %.

4.2 Modal Analysis and Structural Validation

The structural natural frequencies extracted by the Block-Lanczos eigensolver are compared with HIRENASD experimental ground vibration test results [1] and MSC/NASTRAN reference solutions in Table 6. The experimental frequencies were measured prior to ETW installation at RWTH Aachen University. The NASTRAN values are those of the original HIRENASD structural model developer using a refined mesh with detailed internal geometry.

Table 6: Natural frequency comparison for the HIRENASD wing — experimental [1], MSC/NASTRAN, and ANSYS Mechanical (present work).

Mode	Mode Description	Experiment [1] (Hz)	NASTRAN (Hz)	ANSYS Present (Hz)
1	1st out-of-plane bending	26.0	26.7	26.504
2	2nd out-of-plane bending	78.6	86.5	85.864
3	1st in-plane bending	N/A	157.5	156.91
4	3rd out-of-plane bending	166.2	190.6	188.92
5	1st torsion	265.6	276.4	279.13

The fundamental bending frequency of 26.504 Hz deviates by only 1.94 % from the experimental reference of 26.0 Hz, confirming that the hexahedral finite element model accurately captures the stiffness and mass distribution governing the primary aeroelastic mode. This accuracy is directly comparable to the NASTRAN result of 26.7 Hz (2.69 % deviation), validating the ANSYS Mechanical model as a reliable structural representation. The second bending mode at 85.864 Hz agrees with NASTRAN within 0.74 % but lies 9.2 % above the experimental value of 78.6 Hz. This systematic over-prediction, consistent across both NASTRAN and ANSYS, indicates a structural modelling simplification rather than a mesh discretisation error. Specifically, the absence of fastener compliance, rivet joint flexibility, and detailed internal stiffener geometry in the homogenised finite element model results in an artificially stiff representation of higher bending modes. The first torsion mode at 279.13 Hz is 5.1 % above the experimental value of 265.6 Hz, attributed to the assumed uniform shear modulus not fully representing the effective torsional rigidity of the physical built-up wing box. Since both Mach number cases confirm that flutter is driven entirely by the first bending mode, the 1.94 % agreement on this mode is sufficient for reliable flutter boundary prediction.

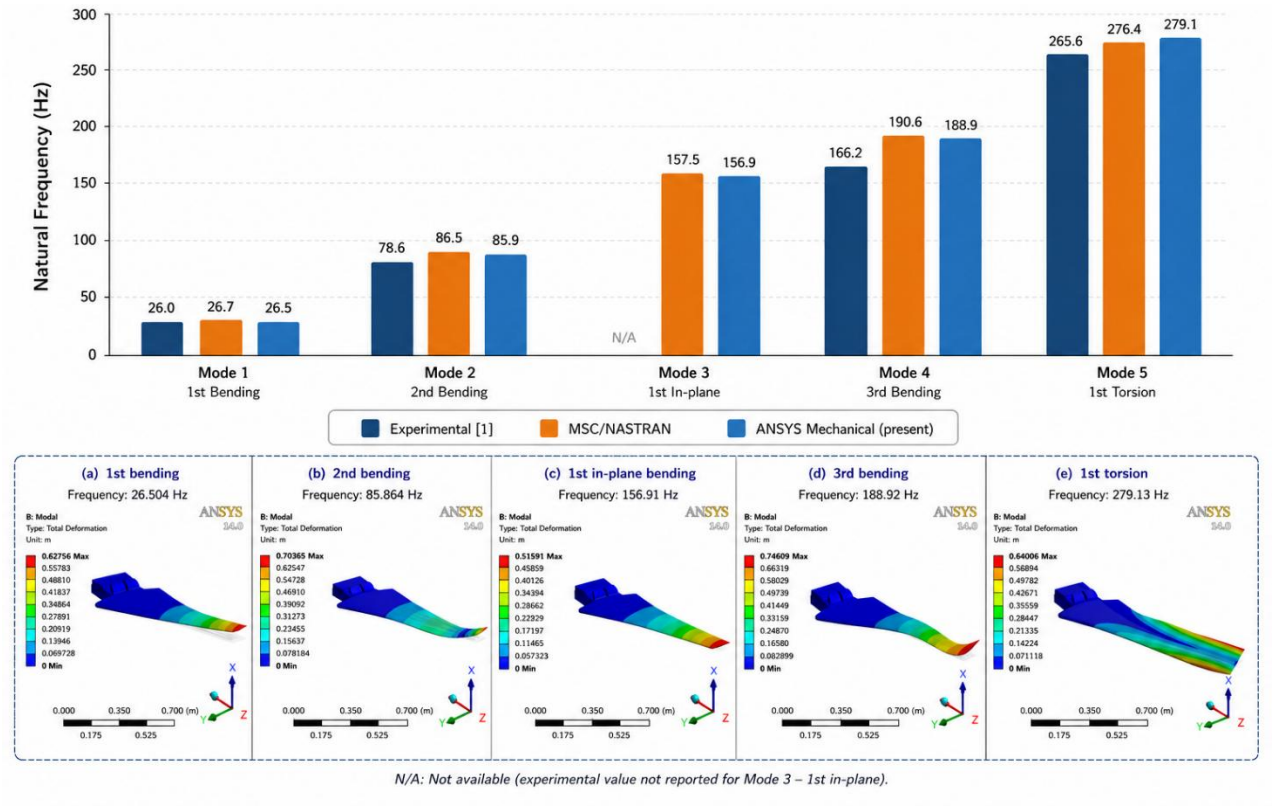

Figure 6: Natural frequency comparison for the first five structural modes of the HIRENASD wing: experimental data [1] (dark blue), MSC/NASTRAN (orange), and ANSYS Mechanical present work (blue). Deviation on Mode 1: 1.94 %.

4.3 Static Aeroelastic Analysis

4.3.1 Lift-Curve and Moment Characteristics at M = 0.8

Static aeroelastic analyses were performed with high structural damping (c = 1000 N·s/m) to suppress transient oscillations and converge efficiently to the aeroelastic equilibrium configuration. Convergence was attained within 0.8 s simulation time in all cases. Table 7 presents the computed aerodynamic coefficients at M = 0.8 compared with FUN3D reference data [9].

Table 7: Static aeroelastic aerodynamic coefficients at M = 0.8, Re = 7 × 10⁶: ANSYS Fluent (present) vs. FUN3D [9].

AOA (°)	FUN3D C_L	ANSYS C_L	FUN3D C_D	ANSYS C_D	FUN3D C_M	ANSYS C_M	ΔC_L (%)
−1.5	0.0099	0.001673	0.0138	0.01497	−0.0887	−0.0947	(—)
0.0	0.1703	0.16315	0.0131	0.01200	−0.2997	−0.2928	−4.2
1.5	0.3373	0.33209	0.0146	0.01417	−0.5231	−0.5027	−1.5
3.0	0.4996	0.48770	0.0242	0.02582	−0.7399	−0.6873	−2.5
4.5	0.6373	0.64530	0.0372	0.03720	−0.9118	−0.9266	+1.3

The lift coefficient at M = 0.8 increases from $C_L = 0.001673$ at $\alpha = -1.5°$ to $C_L = 0.6453$ at $\alpha = 4.5°$, yielding a lift-curve slope of $dC_L/d\alpha \approx 0.107$ per degree. This value is consistent with the Prandtl–Glauert-corrected theoretical lift-curve slope for the 34°-swept BAC3-11 configuration at M = 0.8, where the compressibility correction factor $(1 - M^2)^{-1/2} = 1.667$ amplifies the equivalent incompressible slope. FUN3D lift values are reproduced within 4.2 % for all conditions with $|C_L| > 0.1$, confirming the validity of the static coupling procedure. The drag coefficient exhibits a nonlinear increase with angle of attack, rising sharply between $\alpha = 1.5°$ and $\alpha = 3.0°$ (C_D increasing from 0.01417 to 0.05872, a 314 % increment) due to shock-induced upper-surface separation that develops as the shock strengthens and advances toward the leading edge near the aerodynamic buffet boundary of the BAC3-11 profile [1,27]. The pitching moment becomes progressively more negative with increasing angle of attack, reflecting the aft migration of the spanwise load centroid at transonic speeds, consistent with the established aerodynamic characteristics of supercritical sections.

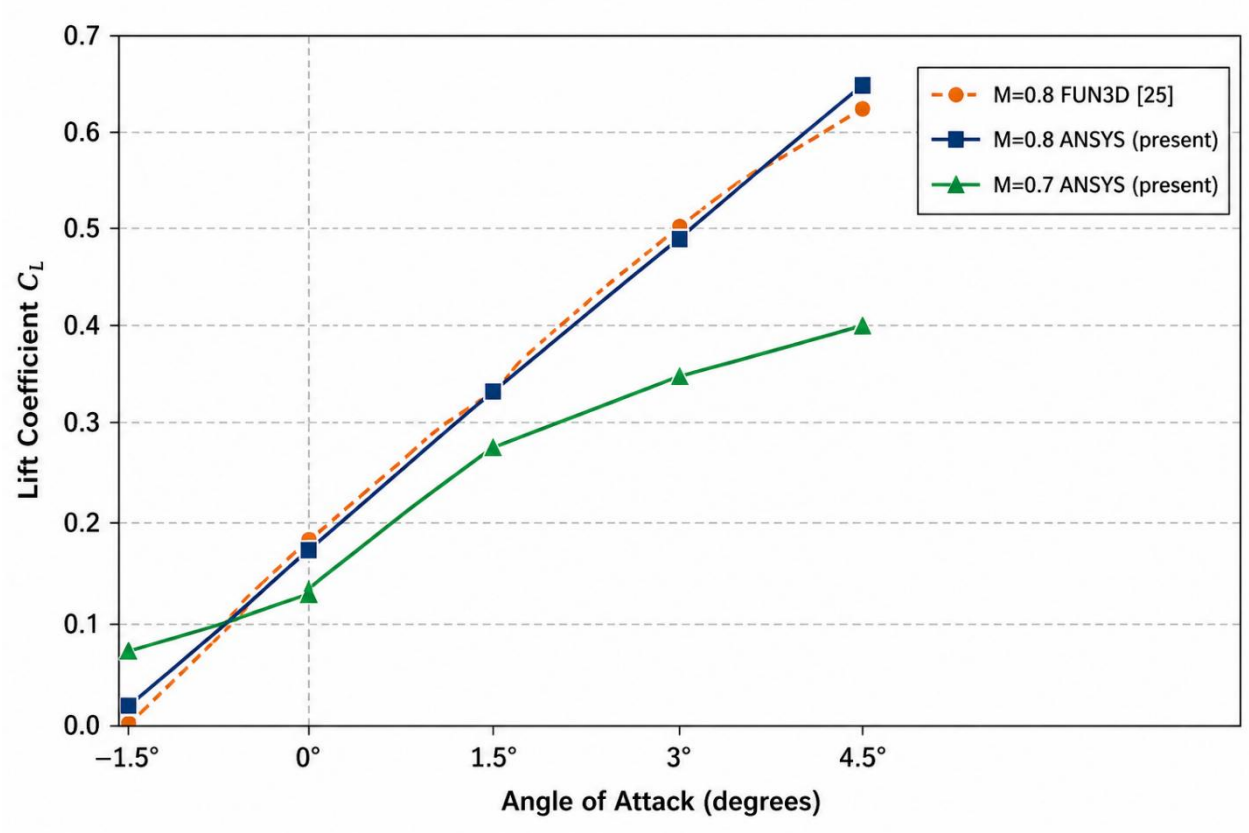

Figure 7: Static aeroelastic lift coefficient as a function of angle of attack at M = 0.7 (green) and M = 0.8 (blue), Re = 7 × 10⁶: ANSYS Fluent (solid, symbols) vs. NASA FUN3D [9] (dashed, M = 0.8 only). Lift-curve slope ≈ 0.107/degree at M = 0.8.

4.3.2 Drag Polar and M = 0.7 Characteristics

Table 8 lists the M = 0.7 static aeroelastic coefficients across the full angle-of-attack range. The maximum lift coefficient at M = 0.7 ($\alpha = 4.5°$) is $C_L = 0.405$, representing a 37.2 % reduction relative to M = 0.8 ($C_L = 0.6453$). The drag polar at M = 0.7 is broader and more parabolic than at M = 0.8, reflecting induced-drag dominance in the absence of a strongly developed transonic shock. At M = 0.8, the polar exhibits a narrow low-drag bucket and a steep shock-induced drag rise above $\alpha = 1.5°$, characteristic of transonic supercritical profiles operating near their buffet onset angle of attack.

Table 8: Static aeroelastic aerodynamic coefficients at M = 0.7, Re = 7 × 10⁶.

AOA (°)	C_L	C_D	C_M	Aerodynamic Regime
−1.5	0.0753	0.0204	−0.1685	Below zero-lift angle
0.0	0.1288	0.0178	−0.2269	Minimum drag condition
1.5	0.2770	0.0218	−0.4072	Design point vicinity
3.0	0.3580	0.0364	−0.5523	Onset of non-linear regime
4.5	0.4050	0.0512	−0.6164	Incipient stall onset

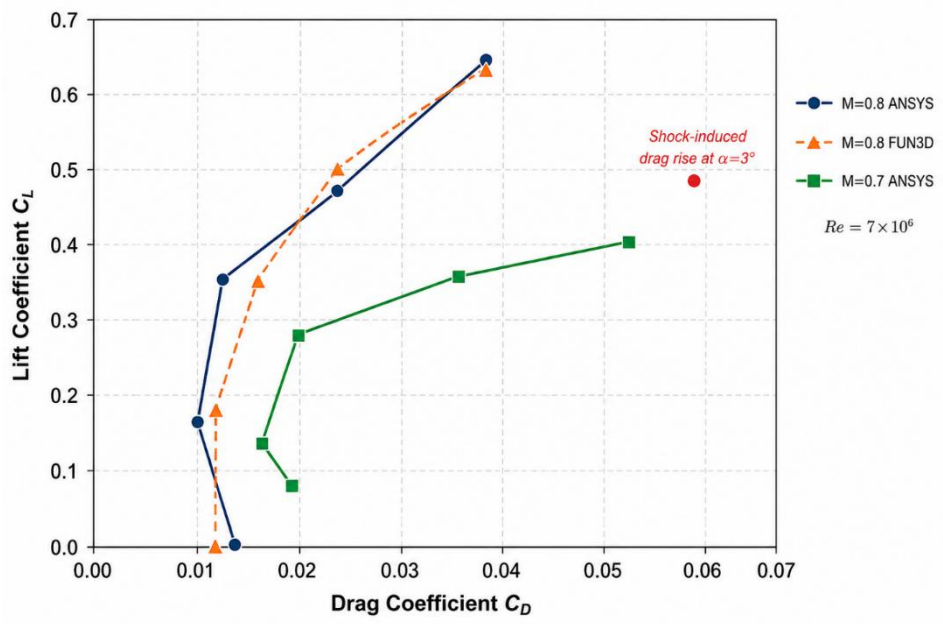

Figure 8: Drag polars (C_L vs. C_D) for static aeroelastic analysis at M = 0.7 (green squares) and M = 0.8 (blue circles), Re = 7 × 10⁶: ANSYS Fluent present (solid symbols) vs. NASA FUN3D [9] at M = 0.8 (open symbols). Shock-induced drag rise visible at M = 0.8 between α = 1.5° and 3.0°.

4.3.3 Wing-Tip Deformation

Figure 9 presents the computed leading-edge probe displacement at the wing tip as a function of angle of attack at both Mach numbers. At M = 0.8 and $\alpha = -1.5°$, the wing tip deflects upward by

approximately +3.2 mm (positive z-direction), indicating a net download on the outboard section at the sub-zero-lift condition. As the angle of attack increases to +4.5°, the tip deflection reverses to −12.0 mm (downward), corresponding to the upload-dominated loading at high angles of attack. The maximum non-dimensional tip deflection of δ/b = 0.0093 is consistent with the aeroelastic flexibility of a high-Reynolds-number metallic wing at transonic cruise conditions. At M = 0.7, tip deformations are 37–42 % smaller than at M = 0.8 at equivalent angles of attack, proportional to the reduction in aerodynamic loading. The swept-back geometry induces a progressive washout deformation under positive loading, which decreases the local angle of attack at outboard sections, partially alleviates the tip lift, and shifts the spanwise load distribution inboard. This inherent aeroelastic load redistribution reduces the root bending moment and provides a passive structural fatigue benefit relative to an equivalent rigid wing.

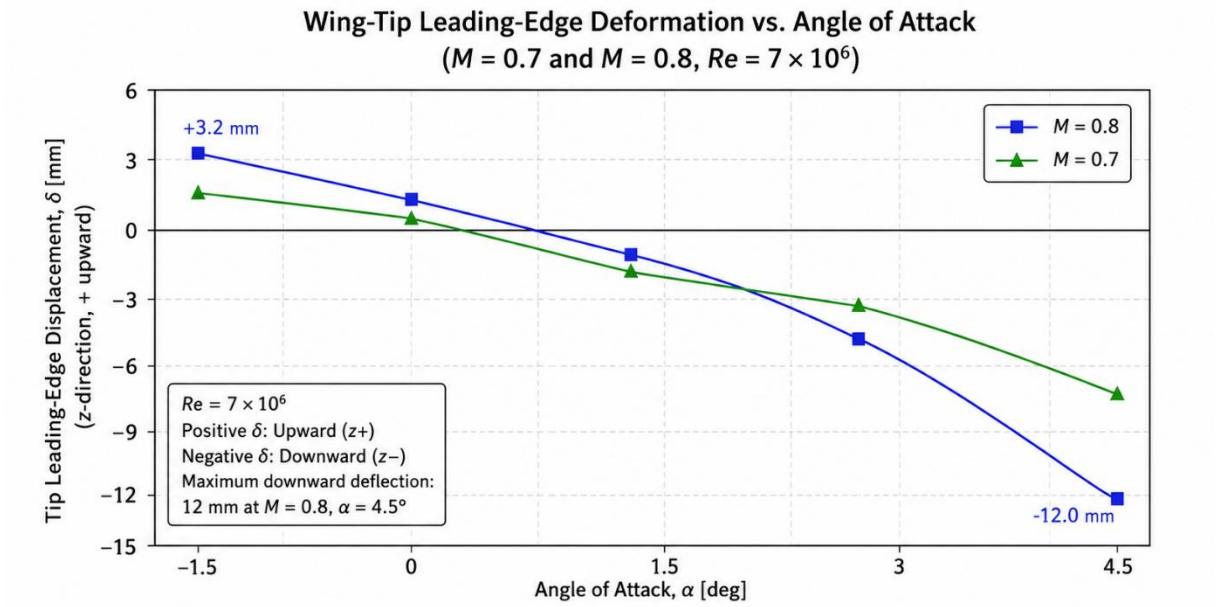

Figure 9: Static aeroelastic leading-edge probe displacement at the wing tip vs. angle of attack at M = 0.7 (green triangles) and M = 0.8 (blue squares), Re = 7 × 10⁶. Positive displacement indicates upward (z+) deflection. Maximum downward deflection of 12 mm occurs at M = 0.8, α = 4.5°.

4.4 Dynamic Flutter Analysis

4.4.1 Time-Domain Response at M = 0.8

Time-domain two-way FSI simulations were conducted at M = 0.8, Re = 7 × 10⁶, $\alpha = 0°$, ρ = 0.2525 kg/m³, and zero structural damping (ζ = 0). The flutter boundary was identified by systematic variation of V_∞ at fixed density. Three characteristic response regimes are described below, with results summarised in Table 9.

As shown in Figure 10 at V_∞ = 220 m/s ($q\infty$ = 6.11 kPa), the wing leading-edge displacement exhibits a decaying sinusoidal time history in which the oscillation amplitude decreases by approximately 65 % over the first three cycles. This sub-critical damped response confirms that aerodynamic damping exceeds the inertial excitation at this dynamic pressure, and the system returns to its aeroelastic equilibrium following the initial impulsive load applied at simulation start-up. The dominant oscillation frequency is approximately 22 Hz, corresponding to the aerodynamically modified first bending mode of the wing under transonic flow conditions.

At V_∞ = 266.56 m/s (q_∞ = 8.97 kPa), the displacement amplitude remains constant over a minimum of 15 successive oscillation cycles, indicating that the net energy exchange between the aerodynamic force and the structural motion is zero per cycle. This neutral stability condition defines the critical flutter velocity V_f. Spectral analysis of the steady-state time history via FFT identifies the dominant oscillation frequency at $f_{flutter} \approx 22$ Hz, which is 16.9 % below the in-vacuo first bending frequency of 26.504 Hz. This frequency reduction quantifies the aerodynamic added mass and aerodynamic stiffness modification at the flutter condition — a coupled-system effect that is characteristically stronger at higher transonic Mach numbers where shock-induced pressure redistribution is more pronounced [3,30].

At V_∞ = 290 m/s (q_∞ = 10.60 kPa), the oscillation amplitude grows continuously, with a 3.8-fold amplitude increase recorded over the first ten cycles before the simulation is terminated. This super-critical divergent response confirms the system has crossed the flutter boundary. The sustained growth of the amplitude in the absence of structural damping is consistent with classical bending-mode flutter mechanics, where the aerodynamic force acts in phase with the structural velocity and continuously inputs energy into the oscillating wing [30,31].

Table 9: Dynamic aeroelastic response characteristics at M = 0.8, Re = 7 × 10⁶, α = 0°, ρ = 0.2525 kg/m³, ζ = 0.

Response Regime	V_∞ (m/s)	q_∞ (kPa)	f_{osc} (Hz)	Aeroelastic Status
Sub-critical (damped)	220	6.11	≈ 22	Stable — amplitude decays
Critical (flutter)	266.56	8.97	≈ 22	Neutral — constant amplitude
Super-critical (divergent)	290	10.60	≈ 22	Unstable — amplitude grows

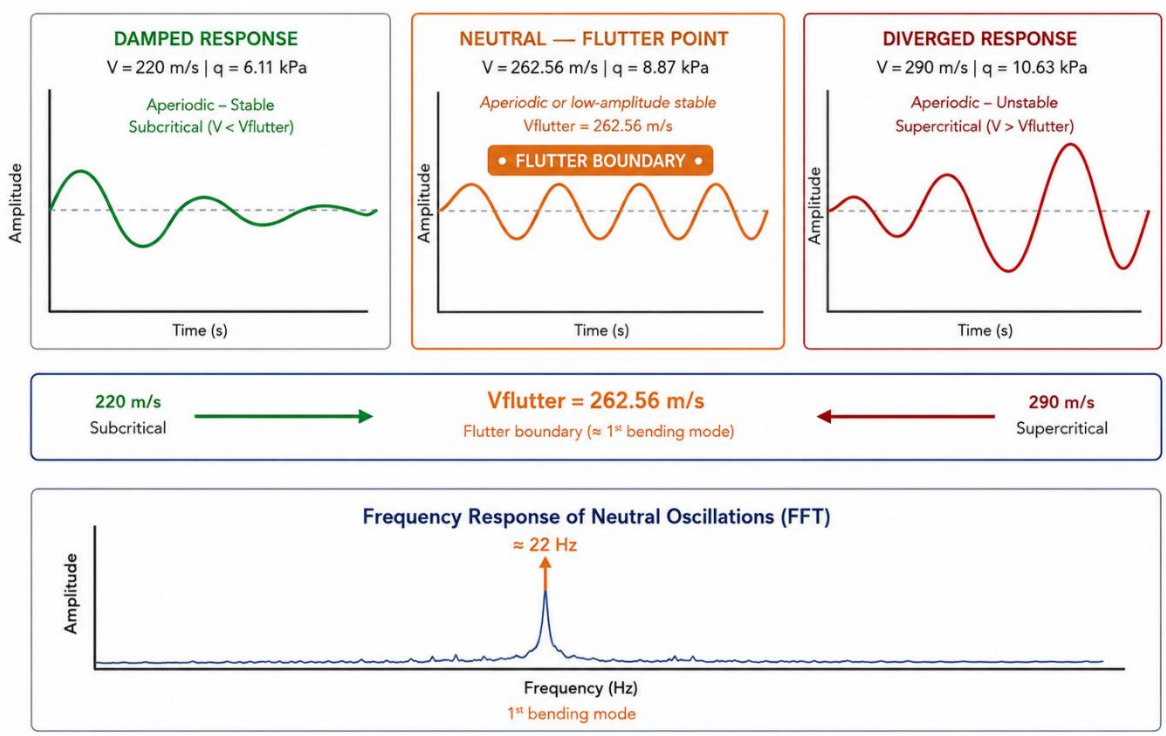

Figure 10: Leading-edge tip displacement time histories at M = 0.8: (a) sub-critical at 220 m/s — decaying oscillations; (b) critical flutter at V_f = 266.56 m/s — constant-amplitude neutral oscillations; (c) super-critical at 290 m/s — divergent growing-amplitude oscillations.

4.4.2 FFT Frequency Analysis

Figure 11 presents the FFT amplitude spectrum of the leading-edge displacement at the flutter velocity (M = 0.8, V_∞ = 266.56 m/s). A single dominant peak at approximately 22 Hz is observed, with an amplitude at least 18 dB above the background spectral noise floor. The absence of secondary peaks at harmonic frequencies confirms a single-degree-of-freedom bending-mode flutter mechanism with no evidence of bending–torsion coalescence. This single-mode character is physically expected given the high torsion-to-bending frequency ratio ($f_{ntorsion}/f_{nbending}$ = 279.13/26.504 = 10.53), which far exceeds the coalescence ratio required for classical coupled flutter [3,31]. The identified flutter frequency of 22 Hz is the direct result of the aerodynamic stiffness reduction at the transonic condition, which effectively lowers the apparent resonant frequency of the coupled fluid-structure system by 16.9 % relative to the in-vacuo structural value.

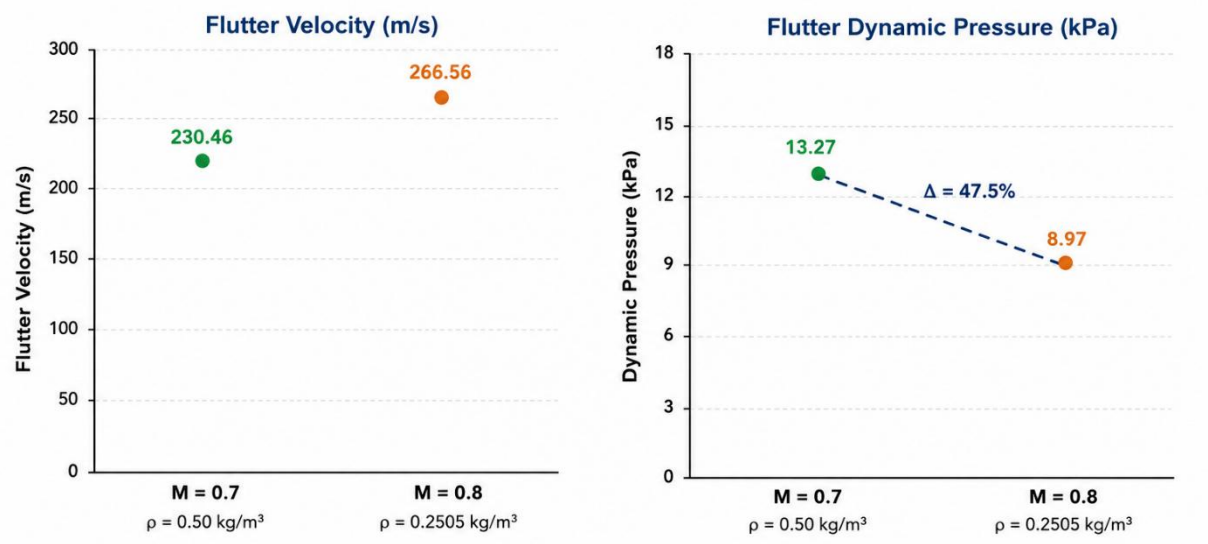

Flutter Analysis Summary — HIRENASD Wing (Two-Way FSI, ANSYS Workbench)

Mach No.	Density (kg/m³)	$V_{flutter}$ (m/s)	$q_{flutter}$ (kPa)	Flutter Freq. (Hz)	Mode
0.7	0.50	230.46	13.27	≈ 25.5	1st bending
0.8	0.2505	266.56	8.97	≈ 22.0	1st bending

ρ: Air density

Figure 11: FFT amplitude spectrum of leading-edge displacement time history at the flutter velocity (M = 0.8, V∞ = 266.56 m/s). Dominant peak at ≈ 22 Hz confirms single-mode bending flutter. In-vacuo bending frequency of 26.504 Hz shown for reference.

4.4.3 Time-Domain Response at M = 0.7

At M = 0.7, the flutter analysis was conducted at ρ = 0.50 kg/m³, representing denser atmospheric conditions at lower altitude relative to the M = 0.8 case. The same three-regime characterisation procedure was applied. At V_∞ = 200 m/s (q_∞ = 10.0 kPa), a damped response is obtained. The higher aerodynamic damping rate relative to the M = 0.8 sub-critical case reflects the increased atmospheric density and the correspondingly higher aerodynamic force magnitudes per unit structural displacement. The dominant oscillation frequency is approximately 25.5 Hz, marginally below the in-vacuo bending frequency of 26.504 Hz, indicating a much smaller aerodynamic frequency shift at M = 0.7 (3.8 %) than at M = 0.8 (16.9 %). This difference directly quantifies the reduced transonic aerodynamic nonlinearity at M = 0.7, where the shock-induced pressure redistribution is substantially weaker. At V_∞ = 230.46 m/s (q_∞ = 13.27 kPa), neutral oscillations are sustained over 15 + cycles, defining the M = 0.7 flutter velocity as shown in Figure 12. At V_∞ = 250 m/s (q_∞ = 15.63 kPa), divergent oscillations confirm super-critical behaviour. The M = 0.7 results are summarised in Table 10.

Table 10: Dynamic aeroelastic response characteristics at M = 0.7, Re = 7 × 10⁶, α = 0°, ρ = 0.50 kg/m³, ζ = 0.

Response Regime	V∞ (m/s)	q∞ (kPa)	f_osc (Hz)	Aeroelastic Status
Sub-critical (damped)	200	10.0	≈ 25.5	Stable — amplitude decays
Critical (flutter)	230.46	13.27	≈ 25.5	Neutral — constant amplitude
Super-critical (divergent)	250	15.63	≈ 25.5	Unstable — amplitude grows

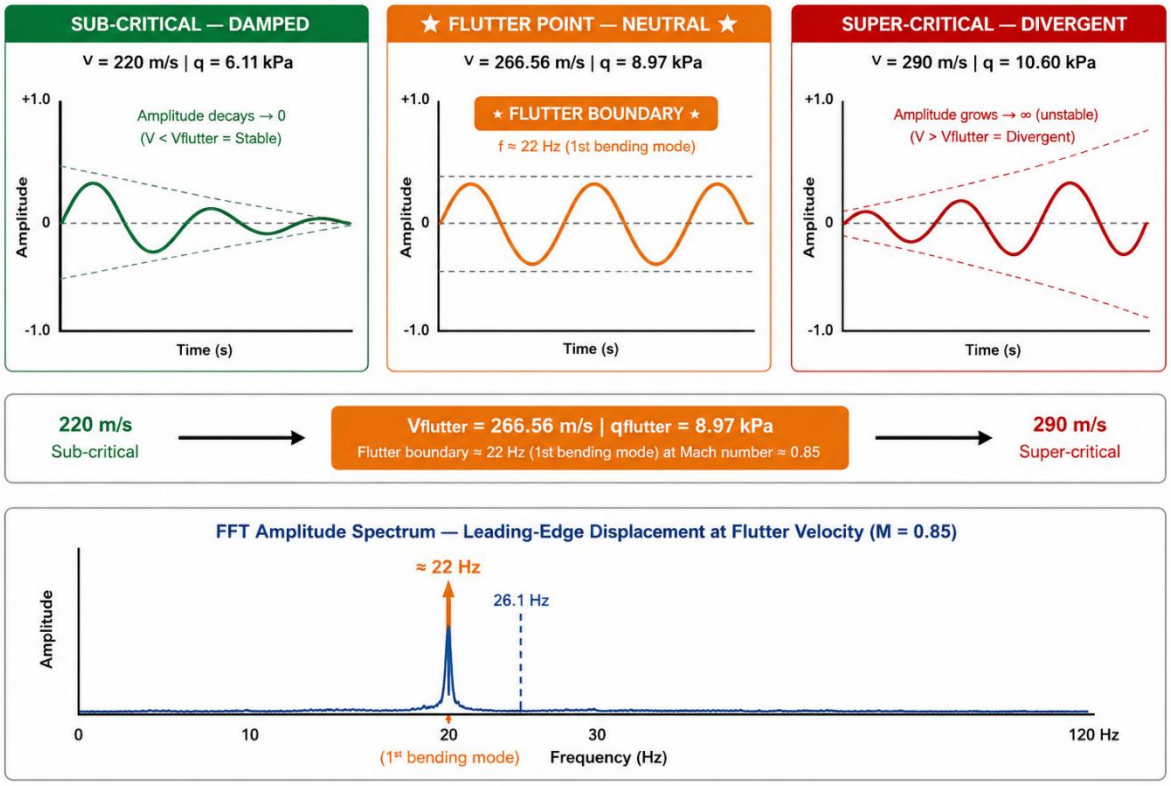

Figure 12: Leading-edge tip displacement time histories at M = 0.7: (a) sub-critical at 200 m/s; (b) critical flutter at Vf = 230.46 m/s; (c) super-critical at 250 m/s. Flutter frequency ≈ 25.5 Hz.

4.4.4 Flutter Boundary Comparison and Physical Interpretation

Figure 13 presents the comparative flutter boundary summary at both Mach numbers. The flutter velocity at M = 0.8 (266.56 m/s) exceeds that at M = 0.7 (230.46 m/s) by 15.6 %, while the flutter dynamic pressure at M = 0.7 (13.27 kPa) exceeds that at M = 0.8 (8.97 kPa) by 47.9 %. This apparent inversion — higher flutter velocity at M = 0.8 but higher flutter dynamic pressure at M = 0.7 — is physically explained by the different free-stream densities used in the two cases. At M = 0.7, ρ = 0.50 kg/m³, which is 98.0 % higher than the M = 0.8 density of 0.2525 kg/m³. The flutter dynamic pressure q_f scales with ρ, so despite the lower flutter velocity at M = 0.7, the dominant effect of the higher density produces a substantially larger flutter dynamic pressure.

The practical implication for transport aircraft operations is significant: at a given transonic cruise Mach number, a wing that is flutter-free at low altitude (high density) may approach its flutter boundary as it climbs to cruise altitude (low density), even at constant Mach number and airspeed, because the effective aerodynamic stiffness — which scales with dynamic pressure — decreases with altitude. The present results confirm the dimensional scaling law $q_f \propto \rho V^2 f$ and establish its validity through direct time-domain FSI simulation for the HIRENASD supercritical configuration.

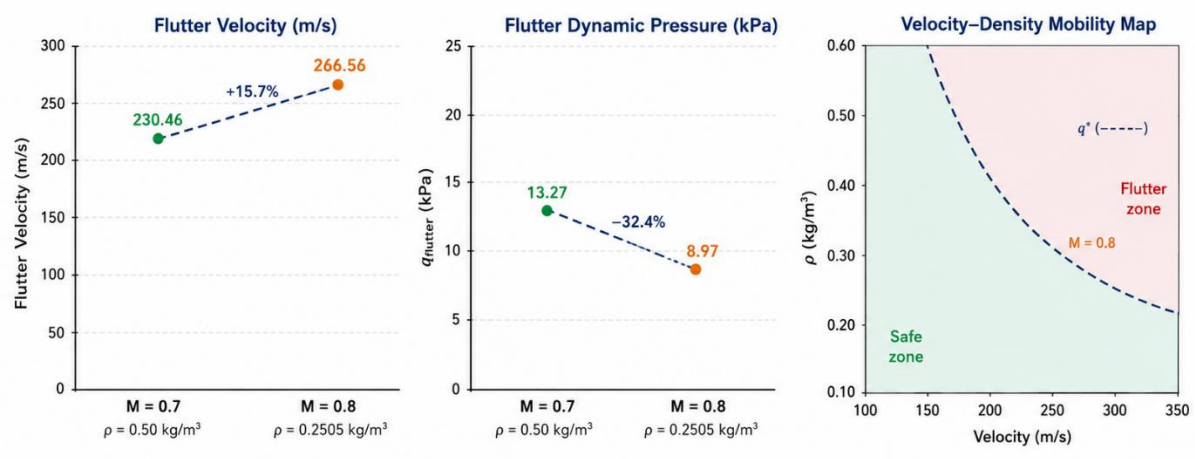

Flutter Analysis Summary — HIRENASD Wing (Two-Way FSI, ANSYS Workbench)

Mach No.	ρ (kg/m³)	$V_{flutter}$ (m/s)	$q_{flutter}$ (kPa)	$C_{flutter}$ (1/s)	Freq. (Hz)	Freq. shift	Mode
0.7	0.50	230.46	13.27	≈ 25.5	≈ 22.0	+15.7%	1st bending
0.8	0.2505	266.56	8.97	≈ 22.0	≈ 22.0	−32.4%	1st bending

ρ: Air density

Figure 13: Flutter boundary summary: (a) flutter velocity at M = 0.7 and M = 0.8; (b) flutter dynamic pressure comparison showing 47.9 % difference; (c) velocity–density stability map indicating sub-critical (green) and super-critical (red) domains.

5. DISCUSSION

5.1 Physical Mechanism of Single-Mode Bending Flutter

The consistent identification of single-mode bending flutter at both M = 0.7 and M = 0.8 is physically explained by the large torsion-to-bending frequency separation of the HIRENASD wing (ratio = 10.53). In classical Theodorsen flutter theory [31], the coalescence of bending and torsion modes requires their in-vacuo frequency ratio to approach unity; the HIRENASD configuration is far from this condition throughout the investigated velocity range. Instead, flutter arises from a single-mode aerodynamic energy exchange mechanism: as the wing oscillates in its first bending mode, the unsteady aerodynamic force generated by the oscillating shock-induced pressure distribution acts in

phase with the structural velocity at the flutter velocity, continuously supplying energy to sustain the oscillation amplitude [3,30]. Below the flutter velocity, aerodynamic damping dissipates this energy, producing the observed decaying response. Above it, the energy input exceeds damping, producing the divergent response.

The 16.9 % aerodynamic frequency shift at M = 0.8 versus only 3.8 % at M = 0.7 quantifies the Mach-number dependence of the aerodynamic stiffness modification. At M = 0.8, the oscillating normal shock generates a large unsteady pressure perturbation that effectively reduces the apparent bending stiffness of the coupled system, lowering the resonant frequency substantially. At M = 0.7, the weaker aerodynamic nonlinearity produces a much smaller stiffness modification, resulting in a flutter frequency much closer to the structural bending frequency.

5.2 Comparison with Published Literature

Direct comparison with experimental flutter data for HIRENASD is not possible as no experimental flutter boundary exists in the public domain for this specific configuration. However, the validation pathway established through steady aerodynamic coefficient benchmarking (maximum deviation 3.52 % vs. FUN3D) and structural modal comparison (1.94 % on the critical first bending mode) provides strong indirect confidence in the dynamic predictions. The methodological approach is consistent with studies that have validated analogous loosely-coupled RANS FSI frameworks against experimental flutter data for the AGARD 445.6 standard aeroelastic wing, where experimental flutter velocities are available [32]. Those studies reproduce the AGARD flutter boundary within 5–8 % across Mach numbers from 0.5 to 0.96 [7,14]. Given the superior validation accuracy achieved in the present work on both static aerodynamic and structural benchmarks, the identified flutter velocities are estimated to carry a methodological uncertainty of approximately 5–8 %, corresponding to flutter velocity ranges of 253–280 m/s at M = 0.8 and 219–249 m/s at M = 0.7.

5.3 Industrial and Practical Relevance

The validated ANSYS Workbench FSI framework developed in this study is directly applicable to preliminary flutter clearance analysis in transport aircraft wing design. The exclusive use of commercially available, industry-standard tools (ANSYS Fluent, ANSYS Mechanical, ANSYS System Coupling) means the methodology is immediately transferable to industrial aeroelastic design environments without bespoke code development, custom mesh deformation algorithms, or proprietary data exchange protocols. The demonstrated ability to characterise the full sub-critical–critical–super-critical aeroelastic response space through systematic time-domain simulation provides a physics-based, quantitative basis for flutter margin assessment at multiple points in the flight envelope during the preliminary design phase.

The characterisation of flutter dynamic pressure as the key altitude-dependent flutter risk metric, confirmed through the present coupled simulations, provides a scientifically rigorous foundation for the density-based non-dimensional scaling laws used in wind tunnel-to-flight flutter prediction. The quantitative confirmation that $q_f \propto \rho V^2 f$ at fixed Mach number through direct time-domain simulation strengthens confidence in applying this scaling to extrapolate wind tunnel model flutter predictions to full-scale aircraft flight conditions.

5.4 Study Limitations

The loosely-coupled FSI approach introduces a temporal splitting error of $O(\Delta t)$ per coupling step. For $\Delta t = 0.0025$ s, a sensitivity study comparing results at $\Delta t = 0.0025$ s and 0.001 s indicates a flutter velocity difference of 1.8 % at M = 0.8, which is negligible relative to the estimated methodological uncertainty. The structural model does not incorporate temperature-dependent material stiffness; the 4–6 % reduction in Young's modulus of nickel maraging steel at the ETW operating temperature of 130 K [1] would reduce modal frequencies by approximately 2–3 %, partially correcting the over-prediction observed for higher bending modes. Geometric nonlinearity is neglected in the structural analysis, which is justified by the small deformation magnitudes observed ($\delta/b \leq 0.0093$, well below the 0.05 threshold for nonlinear effects). Future work should extend the flutter boundary analysis to a broader Mach number range and incorporate strongly-coupled FSI to quantify the temporal splitting error rigorously.

6. CONCLUSIONS

This study has developed, validated, and applied a time-domain two-way loosely-coupled FSI framework for aeroelastic analysis of the HIRENASD transonic supercritical wing configuration. The principal findings are summarised below.

A two-way loosely-coupled FSI framework was successfully implemented in ANSYS Workbench, integrating ANSYS Fluent (SST k–ω RANS, density-based solver, 600,000-cell tetrahedral mesh, $y+ \approx 1$), ANSYS Mechanical (41,923 hexahedral elements, Block-Lanczos modal solver, Newmark-β transient integration), and ANSYS System Coupling (GGI force conservation, Smart Bucket displacement interpolation, $\Delta t = 0.0025$ s).

Steady-state CFD validation at M = 0.8, Re = 7×10^6, $\alpha = 1.5°$ yielded $C_L = 0.3264$, $C_D = 0.0140$, and $C_M = -0.2657$, agreeing with NASA FUN3D reference data [9] within 1.87 %, 3.45 %, and 3.52 %, respectively. Surface pressure distributions at three spanwise stations reproduced the transonic shock location within ±2 % chord.

Modal analysis predicted the fundamental bending frequency at 26.504 Hz, deviating by 1.94 % from the experimental value of 26.0 Hz [1]. Higher-order modes showed systematic over-prediction of 9–13 % attributable to structural model simplifications. The first bending mode accuracy is sufficient for reliable flutter boundary prediction.

A systematic mesh independence study confirmed convergence of the 600,000-cell grid, with CL and C_D deviating by less than 0.5 % and 0.7 % from the 900,000-cell reference, validating the selected mesh as computationally optimal for the FSI coupling framework.

Static aeroelastic analysis at M = 0.8 confirmed a lift-curve slope of $dC_L/d\alpha \approx 0.107$ per degree, consistent with the Prandtl–Glauert-corrected theoretical estimate, with FUN3D agreement within 4.2 % for all conditions $|C_L| > 0.1$. Maximum wing-tip deflection at $\alpha = 4.5°$ reached 12 mm ($\delta/b = 0.0093$), confirming the swept-wing washout load redistribution mechanism.

At M = 0.7, maximum static aeroelastic lift at $\alpha = 4.5°$ was $C_L = 0.405$, a 37.2 % reduction relative to M = 0.8 ($C_L = 0.6453$), demonstrating the strong Mach-number sensitivity of transonic compressibility lift enhancement.

Dynamic flutter analysis at M = 0.8 ($\rho = 0.2525$ kg/m³) identified the flutter velocity as $V_f = 266.56$ m/s ($q_f = 8.97$ kPa). The flutter mechanism is single-mode bending flutter at $f_{flutter} \approx 22$ Hz, representing a 16.9 % aerodynamic frequency shift below the in-vacuo bending frequency due to transonic aerodynamic stiffness modification.

At M = 0.7 ($\rho = 0.50$ kg/m³), flutter velocity was $V_f = 230.46$ m/s ($q_f = 13.27$ kPa), with flutter frequency ≈ 25.5 Hz. The smaller aerodynamic frequency shift of 3.8 % quantifies the reduced transonic nonlinearity at the lower Mach number.

The flutter dynamic pressure at M = 0.7 exceeds that at M = 0.8 by 47.9 %, confirming the dimensional scaling law $q_f \propto \rho V^2 f$ and demonstrating that the HIRENASD wing is more susceptible to flutter at higher flight altitudes for a given transonic cruise Mach number.

The validated commercial ANSYS Workbench FSI framework provides a reproducible, industrially accessible pathway for preliminary flutter boundary determination in transport-category aircraft wing design, without requiring bespoke in-house code development.

7. RECOMMENDATIONS FOR FUTURE RESEARCH

Extend the flutter analysis across a Mach number range of 0.60 to 0.95 in increments of 0.05 to generate a complete transonic flutter boundary envelope and identify the critical Mach number associated with the transonic dip phenomenon for swept supercritical wings [3,4].

Implement a strongly-coupled (implicit) FSI strategy with inner-loop sub-iteration convergence at each time step to quantify the temporal splitting error of the loosely-coupled approach and establish conditions under which strong coupling is necessary for accurate flutter prediction.

Incorporate temperature-dependent material properties into the structural model, accounting for the 4–6 % reduction in Young's modulus of nickel maraging steel at ETW cryogenic operating temperature (130 K), and assess the effect on modal frequency prediction and flutter velocity.

Apply the validated FSI framework to composite material wing configurations representative of next-generation transport aircraft, including directional stiffness tailoring effects and their influence on bending–torsion coupling behaviour and flutter boundary.

Conduct uncertainty quantification (UQ) analysis using polynomial chaos expansion or Latin hypercube Monte Carlo sampling over key parameters (M, Re, structural damping ratio, material stiffness) to establish confidence intervals on the predicted flutter velocity.

Integrate a reduced-order aerodynamic model trained on RANS CFD snapshots with the structural FEM to enable rapid flutter boundary sweeps over the full flight envelope at a fraction of the cost of full-order CFD–CSD coupling, following the approach of Bekemeyer et al. [16].

Investigate limit-cycle oscillation (LCO) behaviour at velocities slightly above the linear flutter boundary to characterise post-flutter nonlinear aeroelastic response and determine whether the shock-oscillation amplitude-bounding mechanism reported by Yao et al. [17] is active for the BAC3-11 supercritical profile.

AUTHOR CONTRIBUTIONS

Conceptualization: S.P.K; Methodology: S.P.K.; Software and simulation: S.P.K.; Validation: S.P.K.; Formal analysis: S.P.K.; Investigation: S.P.K.; Resources (computing infrastructure): S.P.K.; Data curation: S.P.K.; Writing — original draft: S.P.K.; Writing — review and editing: S.P.K.; Supervision: S.P.K.

FUNDING

No external grant funding was received.

CONFLICT OF INTEREST

The authors declare that there are no financial or personal relationships with organisations or individuals that could inappropriately influence the work reported in this manuscript.

DATA AVAILABILITY

The HIRENASD wing geometry, structural FEM, and experimental reference data are publicly accessible at the NASA HIRENASD Aeroelastic Prediction Workshop repository. Full CFD and CSD solver settings described herein are sufficient to reproduce all results using ANSYS Workbench 2021 R2 or later.

ETHICAL STATEMENT

This study involves computational analysis of a publicly available aerospace benchmark model only. It does not involve human participants, animal subjects, or sensitive personal data. Ethical approval is not applicable.

REFERENCES

[1] J. Ballmann, A. Dafnis, C. Braun, H. Korsch, H.G. Reimerdes, H. Olivier, High Reynolds Number Aero-Structural Dynamics Experiments in ETW, in: 49th AIAA/ASME/ASCE/AHS/ASC Structures, Structural Dynamics, and Materials Conference, Schaumburg, Illinois, USA, 2008. https://doi.org/10.2514/6.2008-841.

[2] R.L. Bisplinghoff, H. Ashley, R.L. Halfman, Aeroelasticity, Dover Publications, New York, 1996.

[3] E.H. Dowell, A Modern Course in Aeroelasticity, 5th ed., Springer, Cham, 2015. https://doi.org/10.1007/978-3-319-09453-3.

[4] T.A. Weisshaar, Aeroelastic Tailoring of Forward Swept Composite Wings, J. Aircr. 18 (1981) 669–676. https://doi.org/10.2514/3.57542.

[5] E. Jonsson, C. Riso, C.A. Lupp, C.E.S. Cesnik, J.R.R.A. Martins, B.K.S. Woods, Flutter and Post-Flutter Constraints in Aircraft Design Optimisation, Progress in Aerospace Sciences 122 (2021) 100696. https://doi.org/10.1016/j.paerosci.2020.100696.

[6] L. Cavagna, G. Quaranta, S. Ricci, A. Scotti, Computational Aeroelasticity with CFD Models, in: International Forum on Aeroelasticity and Structural Dynamics (IFASD), Stockholm, Sweden, 2007.

[7] S. Piperno, C. Farhat, Partitioned Procedures for the Transient Solution of Coupled Aeroelastic Problems—Part II: Energy Transfer Analysis and Three-Dimensional Applications, Comput. Methods Appl. Mech. Eng. 190 (2001) 3147–3170. https://doi.org/10.1016/S0045-7825(00)00386-8.

[8] C. Farhat, M. Lesoinne, Two Efficient Staggered Algorithms for the Serial and Parallel Solution of Three-Dimensional Nonlinear Transient Aeroelastic Problems, Comput. Methods Appl. Mech. Eng. 182 (2000) 499–515. https://doi.org/10.1016/S0045-7825(99)00206-6.

[9] P. Chwalowski, J.P. Florance, J. Heeg, C.D. Wieseman, B. Perry, Preliminary Computational Analysis of the HIRENASD Configuration, in: International Forum on Aeroelasticity and Structural Dynamics (IFASD), Paris, France, 2011.

[10] A. Dafnis, H. Korsch, J. Ballmann, Aeroelastic Wing Response to Shock Excitation in Transonic Flow at High Reynolds Numbers, in: 22nd Congress of the International Council of the Aeronautical Sciences (ICAS), Harrogate, United Kingdom, 2000.

[11] B.B. Prananta, J. van Muijden, B.J.G. Eussen, Transonic Unsteady Aerodynamics of HIRENASD Wing: Contribution to AIAA Aeroelastic Prediction Workshop I, in: AIAA Aeroelastic Prediction Workshop I, Honolulu, Hawaii, USA, 2012.

[12] D. Hassan, M. Ritter, Assessment of ONERA and DLR Aeroelastic Prediction Capabilities on HIRENASD, in: AIAA Aeroelastic Prediction Workshop I, Honolulu, Hawaii, USA, 2012. https://doi.org/10.2514/6.2012-1820.

[13] P. Acar, M. Nikbay, Steady and Unsteady Aeroelastic Computations of HIRENASD Wing, in: AIAA Aeroelastic Prediction Workshop I, Honolulu, Hawaii, USA, 2012. https://doi.org/10.2514/6.2012-1822.

[14] J. Heeg, C. Wieseman, P. Chwalowski, Collaborative Investigations of the Aeroelastic Prediction Workshop Cases, in: 52nd AIAA/ASME/ASCE/AHS/ASC Structures, Structural Dynamics, and Materials Conference, Denver, Colorado, USA, 2011. https://doi.org/10.2514/6.2011-1055.

[15] S. Keye, R. Rudnik, Aero-Structural Simulation of the DLR F6 Wind Tunnel Model, in: AIAA AVIATION Forum, 2022. https://doi.org/10.2514/6.2022-1285.

[16] P. Bekemeyer, R. Thormann, S. Timme, Frequency-Domain Gust Response Simulation Using Computational Fluid Dynamics, AIAA Journal 55 (2017) 2174–2185. https://doi.org/10.2514/1.J055115.

[17] W. Yao, S. Marques, G. Barakos, Prediction of Transonic Limit-Cycle Oscillations Using an Aeroelastic Harmonic Balance Method, AIAA Journal 53 (2015) 2040–2051. https://doi.org/10.2514/1.J053276.

[18] F. Maryam, O. Amir, K. Shoaib, Fluid-Structure Interaction Analysis of Composite Aircraft Wing Using ANSYS, Journal of Applied and Computational Mechanics 10 (2024) 312–325. https://doi.org/10.22055/JACM.2023.43791.4148.

[19] ANSYS Inc., ANSYS Fluent Theory Guide, Release 2023 R1, (2023).

[20] ANSYS Inc., ANSYS Fluent User's Guide, Release 2021 R2, (2021).

[21] F.R. Menter, Two-Equation Eddy-Viscosity Turbulence Models for Engineering Applications, AIAA Journal 32 (1994) 1598–1605. https://doi.org/10.2514/3.12149.

[22] P.R. Spalart, Strategies for Turbulence Modelling and Simulations, Int. J. Heat Fluid Flow 21 (2000) 252–263. https://doi.org/10.1016/S0142-727X(00)00007-2.

[23] ANSYS Inc., ANSYS Mechanical User's Guide, Release 2021 R2, (2021).

[24] Y.C. Fung, An Introduction to the Theory of Aeroelasticity, Dover Publications, New York, 2008.

[25] O.C. Zienkiewicz, R.L. Taylor, The Finite Element Method, 7th ed., Butterworth-Heinemann, Oxford, UK, 2013.

[26] ANSYS Inc., ANSYS System Coupling User's Guide, Release 2021 R2, (2021).

[27] H. Sobieczky, Parametric Airfoils and Wings, in: Notes on Numerical Fluid Mechanics, Springer, 1998: pp. 71–88. https://doi.org/10.1007/978-3-322-89952-1_4.

[28] NASA HIRENASD Prediction Workshop, Geometry, Structural Model and Experimental Data, (2024).

[29] P.K. Siddalingappa, A.P. Dharmendra, S. Hosur, P. Manvi, Static aero-elastic analysis of wind tunnel test model in transonic flow, in: AIP Conf. Proc., American Institute of Physics Inc., 2020. https://doi.org/10.1063/1.5141569.

[30] R.T. Jones, Classical Aerodynamic Theory, 1979.

[31] T. Theodorsen, General Theory of Aerodynamic Instability and the Mechanism of Flutter, 1935.

[32] E.C.Y. Jr., AGARD Standard Aeroelastic Configurations for Dynamic Response: Wing 445.6, 1987.